Earth Planet. Sci. Lett. 668 (2025) 119562

Contents lists available at ScienceDirect

Earth and Planetary Science Letters

journal homepage: www.elsevier.com/locate/epsl

The effect of pressure on sulfur valence state in mafic silicate melts

Michelle J. Muth [a,b,*], Elizabeth Cottrell [b]

[a] Department of Earth and Space Sciences, University of Washington, Seattle, WA, 98195 USA
[b] Department of Mineral Sciences, National Museum of Natural History, Smithsonian Institution, Washington DC 20560, USA

ARTICLE INFO

Editor: Dr R. Hickey-Vargas

Keywords:
Redox
Magma
Sulfur
Mantle
Basalts

ABSTRACT

In silicate melts the transition from S^{2-} to S^{6+} occurs over a narrow range of oxygen fugacities (f_{O2}) such that small changes in melt f_{O2} may significantly impact sulfur transport, sulfur mineral/melt partitioning, and sulfur vapor/melt partitioning. The dependence of this transition on pressure remains poorly constrained. Here we present analyses of hydrous sulfur-bearing basaltic-andesite glasses equilibrated at f_{O2} values that span the S^{2-} to S^{6+} transition at 1380 °C at 1.5 and 3 GPa. We have quantified sulfur valence state using S-XANES and estimated f_{O2} from glass $Fe^{3+}/\Sigma Fe$ ratios determined using Fe-XANES and Pt_xFe_{1-x} capsule alloy compositions. We find that the effect of pressure on sulfur valence state is modest at constant absolute f_{O2}. From 1.5 GPa to 3 GPa, the absolute log f_{O2} of the transition from S^{2-} to S^{6+} (defined as log $f_{O2}^{tr\ ans}$) increases by 0.30±0.19 log units. This corresponds to an empirical pressure dependence for absolute log $f_{O2}^{tr\ ans}$ of 0.20±0.13/GPa, a pressure dependence for log $f_{O2}^{tr\ ans}$ of -0.47±0.13/GPa relative to the QFM buffer, and a pressure dependence for log $f_{O2}^{tr\ ans}$ of -0.14±0.13/GPa relative to the FFM buffer, respectively. These results are consistent with previously published thermodynamic calculations. We apply our results to simplified mantle melting and melt extraction models and find that melt $S^{6+}/\Sigma S$ remains relatively constant from 2 to 0.1 GPa. This implies that, unlike the case of $Fe^{3+}/\Sigma Fe$, pressure is not a strong control on melt $S^{6+}/\Sigma S$, and that $S^{6+}/\Sigma S$ measured in primitive, undegassed volcanic glasses broadly reflects the $S^{6+}/\Sigma S$ of melts in their source regions. The corollary is that, while S-free liquids decompress approximately parallel to the QFM buffer, liquids with significant S^{6+}contents will not. In mafic melts, we predict that sulfate is present under the relatively reducing conditions found at mid-ocean ridges. For particularly sulfate-rich magmas, a failure to consider S-Fe redox exchange during ascent could lead to a slight overestimate of f_{O2} on the order of 0.2 log units relative to QFM.

1. Introduction

The chemical behavior of sulfur in Earth's mantle underpins many key geochemical and geodynamic models. Sulfur in fluids, melts, and vapor transports redox budget between Earth's reservoirs and can strongly influence the relationships between tectonic setting and magma chemistry (Luhr et al., 1984; Métrich et al. 1999a; Mungall et al. 2002; Evans 2012; Muth and Wallace 2021; Muth and Wallace 2022). Additionally, the timing and location of sulfide saturation in melts impacts the formation of metal ore deposits (Naldrett and Duke 1980; Richards 2015).

In basaltic melts, sulfur is present in two different valence states, S^{6+} (sulfate) and S^{2-} (sulfide). Sulfur valence state strongly affects conditions in which melts saturate in sulfides (Jugo et al. 2010), solubility of sulfur in magmatic vapor (Luhr et al. 1990; Ding et al. 2023; Hughes et al. 2023), and redox exchange between sulfur and other redox-sensitive elements such as iron (Carmichael and Ghiorso 1986). The proportion of S^{6+} and S^{2-} (commonly expressed as $S^{6+}/\Sigma S$, where $\Sigma S = S^{6+} + S^{2-}$) varies as a function of melt oxygen fugacity (f_{O2}).

Melt $S^{6+}/\Sigma S$ increases rapidly over a narrow interval of increasing log f_{O2} (Carroll and Rutherford 1988; Wallace and Carmichael 1994) but this broad understanding has continued to undergo refinement due to the importance of sulfur redox to Earth processes. Experiments at crustal (200 MPa) pressures (Jugo et al. 2010; Botcharnikov et al. 2011) and measurements of natural volcanic glasses (Brounce et al., 2017; Muth and Wallace 2021; Saper et al., 2024b) show that basaltic and andesitic melts transition from S^{2-}-dominated to S^{6+}-dominated at approximately $\Delta QFM = 1$ (where QFM is the quartz-fayalite-magnetite buffer). For convenience, we define this S valence transition point where $S^{6+}/\Sigma S = 0.5$ as $f_{O2}^{tr\ ans}$. One-atmosphere experiments have allowed authors to more accurately model how $f_{O2}^{tr\ ans}$ shifts with melt composition and temperature (O'Neill and Mavrogenes 2022; Boulliung and Wood 2023)

* Corresponding author.
E-mail address: mmuth@uw.edu (M.J. Muth).

https://doi.org/10.1016/j.epsl.2025.119562
Received 25 March 2025; Received in revised form 22 July 2025; Accepted 28 July 2025
Available online 7 August 2025

as well as kinetics (Saper et al., 2024a). Relationships between melt $S^{6+}/\Sigma S$ and $Fe^{3+}/\Sigma Fe$ remain constant over a wide range of quench rates, meaning that we can more confidently interpret measured $S^{6+}/\Sigma S$ in a wide variety of natural and experimental glasses (Muth and Cottrell, 2023). However, the effect of pressure on $f_{O2}^{tr\_ans}$ is poorly constrained experimentally.

Current uncertainty in f_{O2}^{trans} inhibits our ability to understand chalcophile elements in magmatic systems. This is because the total sulfur content at sulfide saturation ($SCSS^T$) is strongly dependent on melt $S^{6+}/\Sigma S$ (Jugo et al., 2010). Most experiments about sulfide stability at mantle pressures were conducted in reducing, S^{2-}-dominated conditions (e.g., Mavrogenes and O'Neill 1999; Holzheid and Grove 2002) and therefore cannot be applied to S^{6+} -bearing melts without information about $f_{O2}^{tr\_ans}$ (e.g., Jugo et al., 2010).

Models constraining $f_{O2}^{tr\_ans}$ come to different conclusions about the effect of pressure. Models fit to sulfur concentrations in a hydrous trachyandesitic glass across a range of f_{O2} suggests that the pressure dependence of $f_{O2}^{tr\_ans}$ is approximately +0.6 log units/GPa relative to QFM. (Matjuschkin et al. 2016; QFM pressure dependence calculated using Frost 1991). The thermodynamic model of Moretti and Baker (2008) suggests that in tholeiitic melts with 0.5 wt. % H_2O, the pressure dependence of log f_{O2}^{trans} is approximately +0.1 log units/GPa relative to QFM. In contrast, the thermodynamic calculations of Boulliung and Wood (2023) suggest the pressure dependence of log f_{O2}^{trans} is approximately −0.3 log units/GPa relative to QFM. Direct measurements of $S^{6+}/\Sigma S$ in experimental products are only available at relatively low (up to 200 MPa) pressure (Jugo et al. 2010; Botcharnikov et al. 2011; Nash et al. 2019; Saper et al., 2024a), which makes it difficult to reconcile these disparate results.

Here, we present a series of hydrous, S-bearing, basaltic-andesite glasses equilibrated in a piston cylinder at 1.5 and 3.0 GPa and 1380 °C. We estimate that the log f_{O2} of these experiments ranges from approximately $\Delta QFM = -2.1$ to $\Delta QFM = 2.3$ based on glass $Fe^{3+}/\Sigma Fe$ ratios determined using Fe- X-ray Absorption Near Edge Structure (XANES) spectroscopy and Pt_xFe_{1-x} capsule alloy compositions. We constrain the S valence transition f_{O2} by measuring $S^{6+}/\Sigma S$ using S K-edge XANES spectroscopy.

2. Methods

2.1. Experiments

We designed our experiments to equilibrate hydrous (1.3 to 6.8 wt. % H_2O), vapor undersaturated, S-bearing (41–4303 ppm) basaltic andesite melt over a range of f_{O2} that would span the S^{2-} to S^{6+} transition. We created Pt-Fe alloy capsules for each experiment with a specific composition designed to minimize Fe-loss and maintain a target f_{O2} (e.g., Davis and Cottrell, 2021). See Supplementary Text for detailed discussion of capsule pre-saturation technique and calculations. After pre-saturation, we dissolved the capsules out of the mixture of magnetite and sodium metasilicate using baths of hydrochloric acid. We coned the end of each capsule, filled it with starting powder, and then sealed the capsule with a tri-crimp weld using a PUK welder. In a subset of capsules that were very brittle due to high concentrations of Fe, we coned the pure Pt capsules on one side before equilibrating them in the furnace, then sealed them as described above after pre-saturation.

The starting composition of our experiments is basaltic andesite (~52 wt. % SiO_2; Table 1) modeled after that of Botcharnikov et al. (2011). This composition was chosen to avoid quench crystallization and provide a means of direct comparison to sulfur-bearing experiments at other P-T conditions. Botcharnikov et al. (2011) showed that this basaltic andesite composition has the same $f_{O2}^{tr\_ans}$ as a basalt under the same P-T conditions (Jugo et al. 2010). We conducted experiments using starting materials with a range of $Fe^{3+}/\Sigma Fe$ and $S^{6+}/\Sigma S$ ratios designed to be in equilibrium with a range of capsule alloy compositions. See Supplementary Text for detailed discussion of starting mix calculations and preparations.

Experiments were conducted in half-inch piston-cylinder apparatuses at the National Museum of Natural History, Smithsonian Institution. Assemblies comprised MgO spacers, a straight-walled graphite furnace, $BaCO_3$ pressure sleeves, and an outer layer of Pb foil. Temperature was controlled using a type-D thermocouple. Experiments were pressurized using a modification of the cold-piston-in technique and pressure calibration described in Andrys et al. (2024). All experiments were conducted for 4–6.5 h at 1380 °C, except for one 1-hour experiment conducted as part of a time series. One set of experiments was conducted at 1.5 GPa, and one set was conducted at 3 GPa. After each experimental run, we mounted each experimental assembly in epoxy and then vertically sectioned it. One side was singly polished and used for EPMA (Electron Probe Micro-Analysis) and XANES (X-ray Absorption Near Edge Structure). The other side was prepared as a doubly polished wafer for FTIR (Fourier Transform Infrared Spectroscopy).

2.2. Analytical methods

We measured each experiment's H_2O and CO_2 content using FTIR. Each wafer was analyzed on a Thermo Scientific Nicolet 6700 FT-IR spectrometer interfaced with a Continuum IR microscope at the National Museum of Natural History, Smithsonian Institution. We measured the major element compositions and sulfur concentration of each glass using EPMA on the JXA-8530FPlus HyperProbe Electron Probe Microanalyzer at the National Museum of Natural History, Smithsonian Institution. We measured $Fe^{3+}/\Sigma Fe$ ratios using Fe-XANES at station 13-ID-E at the Advanced Photon Source (APS), Argonne National Laboratory, USA and at station 4-BM XFM at the National Synchrotron Light Source (NSLS) II, Brookhaven National Laboratory. We measured $S^{6+}/\Sigma S$ values using S-XANES at APS. See Supplementary Text for detailed description of analytical conditions and beam damage mitigation approaches for each technique.

3. Results

3.1. Experimental products

All experiments contained crystal-free glass except for experiments PC361 and PC360 at 3 GPa, which contain small amounts of clinopyroxene and garnet crystals at the bottom (cold end) of the capsule. No sulfides were observed in the glass pools of any experiments. In experiments with a high starting concentration of sulfur, we observe one or more ~10–100 μm diameter PtS blebs hosted within the Pt_xFe_{1-x} capsule (e.g., Fig. 1). In some experiments, capsules show clear textural signs of brittle fracture but display no evidence of rupture or leakage at experimental conditions. Fractures in the capsule tend to form along alloy grain boundaries and parallel to the decompression cracks found ubiquitously in piston cylinder charges. This texture is consistent with the well-documented effect of sulfur-induced embrittlement in metal alloys (Christien, 2020), where sulfur-bearing exsolution phases cause dynamic embrittlement. This embrittlement occurs even in alloys with

Table 1
Experiment starting composition in weight percent.

SiO_2	TiO_2	Al_2O_3	FeO^T	MnO	MgO	CaO	Na_2O	K_2O	H_2O	S[a]
52.3	2.4	16.0	6.6	0.2	3.7	7.7	3.2	2.8	4.1	0.1–1.2

[a] S concentrations varied from 1,000 to 12,000 ppm S (see Supplementary Text for details).

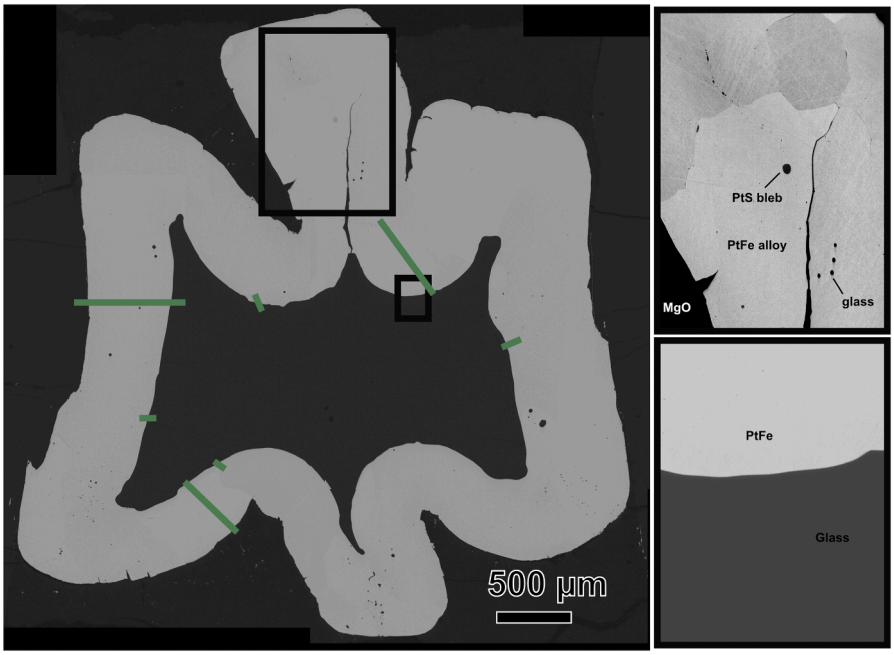

Fig. 1. Backscatter electron image of experiment PC349. The top inset was taken with high contrast to show PtFe alloy grains. The bottom inset shows the contact between glass and Pt_xFe_{1-x} alloy, where no reaction products are shown. Green bars show areas where EPMA transects of Pt, Fe, and Mg concentration were taken. Transect values are in Supplemental Table 6, and plots showing transect results are shown in Supplementary Figure 1.

very small (i.e. 5–30 ppm) concentrations of sulfur. We do not find any evidence that capsules breached prior to quench nor that the melt interior was contaminated during these experiments, and we do not exclude these experiments in the present study.

3.2. Glass and capsule compositions

We report the major element compositions of all experiments in Supplementary Table 5. A subset of experiments with longer (~3 mm) experimental charges (PC346, PC353, PC357, PC358, PC362) are vertically compositionally zoned in a manner consistent with Soret diffusion caused by a temperature gradient across the capsule (Walker and DeLong 1982). We define this subset as those having correlations between glass depth from the capsule top and glass SiO_2 content with $R^2 > 0.5$ (Supplementary Figure 10). Compositions in these experiments vary by ~1–2 wt. % in SiO_2 and patterns in major element composition with depth indicate that the bottom of these experiments was slightly below the assembly hot spot. All experiments contain between 4.6 and 6.8 wt. % H_2O, except for experiments PC351 and PC349, which contain 1.8 and 1.3 wt. % H_2O. Experiments also contain significant carbon dissolved as CO_3^{2-}, ranging from 0.1 to 1.3 wt. % CO_2. We believe that decarbonation of the starting materials was complete; we note that CO_2 is commonly reported (whenever measured) as a glass contaminant in piston cylinder experiments (e.g., Brooker et al. 1998; Gaetani and Grove 1998; Liu et al. 2006). We have no reason to suspect that carbonate contamination affected our results. Melt $S^{6+}/\Sigma S$ in our experiments varies from 0.02 to 0.99. Melt $Fe^{3+}/\Sigma Fe$ varies from 0.05 to 0.23. See Supplementary Table 5 for analyses of glass $Fe^{3+}/\Sigma Fe$ and $S^{6+}/\Sigma S$ values of each experiment.

Measured glass concentrations of total iron (FeO*) range from 3.58 to 6.93 wt. % across all experiments. Change in glass total iron from the initial starting powder iron content ranged from −15 % to −20 % at 1.5 GPa and from −31 % to −48 % at 3 GPa. Sulfur contents range from 41 to 4303 ppm. Experiments with the highest sulfur contents (HG60 and PC340) are sulfate-dominated, which likely mitigated sulfur loss as PtS blebs within the Pt_xFe_{1-x} alloy capsules. Change in glass total sulfur from initial starting sulfur content ranged from −99 % to −56 % at 1.5 GPa, and from −97 % to −91 % at 3 GPa. Average sulfur content, excluding HG60 and PC340, is 196±90 ppm. Average standard deviation of 5–7 analyses on each glass is 22 ppm.

Sulfur in the Pt_xFe_{1-x} alloy capsules is below the detection limit using EPMA, although the detection limit in our analyses is relatively high (~800 ppm) due to the interference of the Pt Mβ peak with the S Kα peak. Given the large mass of the capsule material relative to the glass interior and the stability of PtS sulfides, it is unsurprising that the loss of sulfur from the melt does not lead to high sulfur contents in the capsule Pt_xFe_{1-x} alloy.

3.3. Approach to equilibrium and conservation of fe and S

We conducted experiments with the same starting composition and the same batch of pre-equilibrated capsules for 1 and 4 h (PC343 and PC344, respectively), to approximate a time series (Supp. Fig. 5). S- and Fe-loss in both experiments are the same within error (86 % and 90 % Fe-loss 12 % and 13 % S-loss). S-loss is consistent with the PtS blebs observed in a subset of experiments as described above. Because PtS blebs are only occasionally observed and vary in size, we cannot confidently estimate how much S is hosted in the PtS blebs. f_{O2} calculated using melt-alloy equilibria and melt $Fe^{3+}/\Sigma Fe$ are also the same within uncertainty between both experiments. These results indicate that after an hour, the melt and melt-alloy interface approach equilibrium at these temperatures. We conservatively chose to run 4- to 6.5-hour experiments.

Because the alloy capsule interiors are more Pt-rich, disproportionation of FeO into Fe^{3+}(melt) and Fe^0 (alloy) is expected to continue throughout the duration of experiments as the capsule concentration gradient relaxes, but local equilibrium between the melt and melt-capsule interior is maintained (Davis and Cottrell, 2021). $S^{6+}/\Sigma S$, and $Fe^{3+}/\Sigma Fe$, and FeO* of the quenched glasses are homogenous in all experiments (Supp. Figs. 1–4) indicating that the timescale of major element diffusion in the melt was faster than, or able to keep pace with, Fe melt/alloy exchange. Additionally, both experiments record broadly consistent offsets between f_{O2} calculated via Fe-XANES and the f_{O2} calculated from capsule alloy composition (Fig. 2; see section

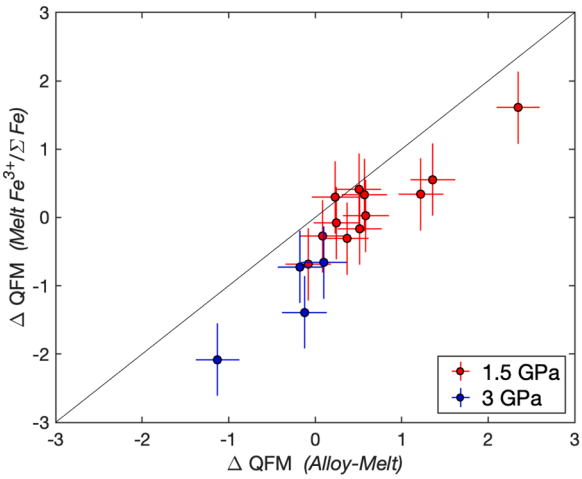

Fig. 2. Oxygen fugacity for each experiment relative to QFM buffer (ΔQFM) was estimated in two ways: (1) from the glass composition and glass $Fe^{3+}/\Sigma Fe$ measured via Fe-XANES (*'Melt $Fe^{3+}/\Sigma Fe$'*) and (2) from the glass composition and the Pt_xFe_{1-x} alloy composition (*'Alloy-Melt'*). Error bars represent 2 sigma combined measurement and calibration uncertainty. 1:1 line shown in black for comparison. Equivalent figures using other algorithms for the relationship between $Fe^{3+}/\Sigma Fe$ and f_{O2} are shown in Supplementary Figure 8.

Determination of experiment f_{O2} for more detail). These observations indicate that, although the melt and capsule continuously exchanged material on the timescale of our experiments, the melt maintained equilibrium with the Pt_xFe_{1-x} alloy capsule edge in contact with the melt.

3.4. Determination of experiment f_{O2}

We determined the f_{O2} of each experiment using two different approaches. We used glass $Fe^{3+}/\Sigma Fe$ values to calculate f_{O2} according to the model of Borisov et al. (2018), using the pressure term of Kress and Carmichael (1991), at the temperature and pressure of each experiment. Experiment log f_{O2} values calculated in this manner ranges from ΔQFM $= -2.1 \pm 0.53$ to ΔQFM$= 1.2 \pm 0.53$, where uncertainty is the standard error of regression of Borisov et al. (2018) for MORB (Mid-ocean ridge basalt)-like basalts (Cottrell et al., 2021). The choice of algorithm to relate $Fe^{3+}/\Sigma Fe$ values to log f_{O2} does not impact our conclusions (Supp. Fig. 8).

Although in a subset of experiments there is small but observable compositional zoning within the glass the effect of these compositional variations on the model of Borisov et al. (2018) is negligible. We do not see any gradients in $Fe^{3+}/\Sigma Fe$ or $S^{6+}/\Sigma S$ across each glass (Supp. Figs. 3 and 4), consistent with models that predict that these small compositional differences would not create measurable differences in $Fe^{3+}/\Sigma Fe$ or $S^{6+}/\Sigma S$ at a given f_{O2} (Borisov et al., 2018; Boulliung and Wood 2023). Relatedly, at a constant melt $Fe^{3+}/\Sigma Fe$ the range of calculated f_{O2} in zoned glasses is negligible. For experiment PC360 (the most strongly zoned experiment; Supp. Fig. 10), log f_{O2} calculated using glass composition at the top and bottom of the capsule differs by 0.03 log units – an order of magnitude less uncertainty than is contributed by uncertainty in the empirical relationship between composition and log f_{O2}.

We also calculated f_{O2} based on the Pt_xFe_{1-x} alloy composition. This method is based on the equilibrium reaction between the alloy and melt below

$$Fe_{alloy} + 1/2O_2 = FeO_{melt} \quad (1)$$

Oxygen fugacity can be calculated using this reaction by considering the equilibrium constant

$$K = \frac{a_{FeO}^{melt}}{a_{Fe}^{alloy} \times f_{O_2}^{\frac{1}{2}}} \quad (2)$$

We calculated the activity coefficient of Fe in the Pt_xFe_{1-x} alloy (γ_{Fe}^{alloy}) using Hirschmann and Zhang (2023) instead of the γ_{Fe}^{alloy} from Kessel et al. (2001). Consistency required that we re-regress data from Médard et al. (2008) with the Pt-Fe solution model of Hirschmann and Zhang (2023) to obtain updated coefficients to their equation (4) for our f_{O2} calculation ($a = -6.144$, $b = 28{,}252$, Fred Davis, pers. comm.). Equation 4 of Médard et al. (2008) integrates the activity coefficient γ_{FeO}^{melt} into the formulation of equilibrium coefficient so that the input from our data is X_{FeO}^{melt} (calculated on a hydrous basis) and γ_{Fe}^{alloy} calculated using Hirschmann and Zhang (2023). Experiment log f_{O2} values calculated with the updated regression range from ΔQFM $= -1.1 \pm 0.3$ to Δ QFM $= 2.3 \pm 0.3$ where uncertainty is combined analytical and model uncertainties. We propagate standard error of the updated regression for equation 4 of Medard et al. (2008) (Davis, pers comm) to calculate model uncertainty.

The effect of compositional heterogeneity on melt-alloy f_{O2} calculations is small but non-negligible. For example, the average standard deviation of capsule-glass interface X_{Fe}^{alloy} across all experiments is $1\sigma = 0.004$, and this creates an uncertainty in log f_{O2} of 1 $\sigma = 0.1$ log units. To ensure that our EPMA analyses of the capsule for melt-alloy f_{O2} calculations represent the alloy in equilibrium with melt during the experiment, we analyzed transects of Fe, Pt, and Mg concentration across the melt-alloy interface on each capsule's top, bottom, and sides. We selected the analysis closest to the interface with MgO below detection and totals over 99 % as most representative of this equilibrated composition (Supp. Fig. 1, 2). We conducted 3–5 transects in different regions of the capsule-glass interface to obtain a mean value for each experiment. In two experiments with capsules >2 mm in length (PC360 and PC361), values of X_{Fe}^{alloy} on the bottom of the capsule were ~0.03 lower than on the top part of the capsule. In these cases, we only use analyses from the top of the capsule, adjacent to the thermocouple, to ensure that the temperature term in our calculation of f_{O2} is accurate.

There is a systematic offset between values derived from the two methods (Fig. 2), with the alloy recording experiment log f_{O2} about 0.4 log units, on average, higher than that calculated from the $Fe^{3+}/\Sigma Fe$ ratio of the glass. In each method, there is uncertainty about the potential effect of sulfur on the calculation of f_{O2}, in the melt and the alloy, which we detail below. The experimental results of Saper et al. (2024a), indicate that the presence of sulfur in melt possibly leads to a lower melt $Fe^{3+}/\Sigma Fe$ at any given f_{O2}. The experiments do not indicate the mechanism (e.g., increase in a_{FeO}^{melt} or decrease in $a_{Fe_2O_3}^{melt}$), and it is not clear why both S^{2-} and S^{6+} should equally stabilize Fe^{2+} over Fe^{3+} in silicate melts. Nevertheless, the Saper et al. (2024a) result suggests that a formulation like Kress and Carmichael (1991) or Borisov et al. (2018), based on sulfur-free melts, may underpredict calculated f_{O2}.

In the case of experiment f_{O2} calculated using the Pt_xFe_{1-x} alloy composition, interactions with sulfur and the alloy and melt may affect a_{Fe}^{alloy} and/or a_{FeO}^{melt}. The concentration of sulfur in the Pt_xFe_{1-x} alloy is below detection, consistent with the Pt-Fe-S ternary (Raghavan 2004). We therefore focus on the effect of sulfur in the melt. If melt a_{FeO}^{melt} decreases with the addition of sulfur, as the experiments of Saper et al. (2024a) suggest could be the case, we would expect this calculation to overpredict f_{O2}. Therefore, while we do not have the complete activity-composition data to know which method for estimating experiment f_{O2} is more accurate, we anticipate the observed directional offset between the two methods employed and confidently bracket the f_{O2} of each experiment.

3.5. Relationship between $S^{6+}/\Sigma S$ and absolute f_{O2} at 1.5 and 3 GPa

In experiments at both 1.5 GPa and 3 GPa, $S^{6+}/\Sigma S$ increases with increasing experiment f_{O2} following an exponential relationship, consistent with predictions from thermodynamic calculations, natural observations, and experimental data at lower pressure (Fig. 3; Carroll and Rutherford 1988; Wallace and Carmichael 1994; Brounce et al.,

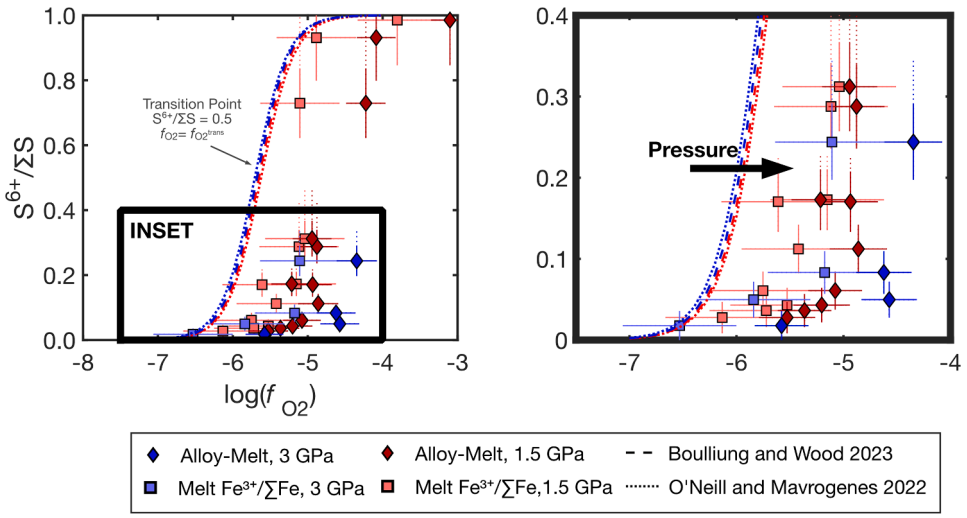

Fig. 3. Sulfur valence state ($S^{6+}/\Sigma S$) and oxygen fugacity (f_{O2}) of experiments at 1380 °C and 1.5 GPa (red) and 3 GPa (blue). We define the inflection point on the speciation curve, f_{O2}^{trans}, as the f_{O2} where $S^{6+}/\Sigma S = 0.5$. Oxygen fugacity for each experiment is estimated in two ways: (1) from the glass composition and glass $Fe^{3+}/\Sigma Fe$ measured via Fe-XANES (squares) and (2) from the glass composition and the PtFe alloy composition (diamonds). Solid vertical error bars represent 2 sigma combined measurement uncertainty, and dashed error bars are calibration uncertainty as described in the text. Dashed model curves are the model of Boulliung and Wood (2023), calculated using the average major element composition of all experiments at 1 atm, 1380 °C. The dotted lines are models of O'Neill and Mavrogenes (2022) under the same conditions. The inset on the right shows a detailed view of S^{6+}- poor experiments for clarity.

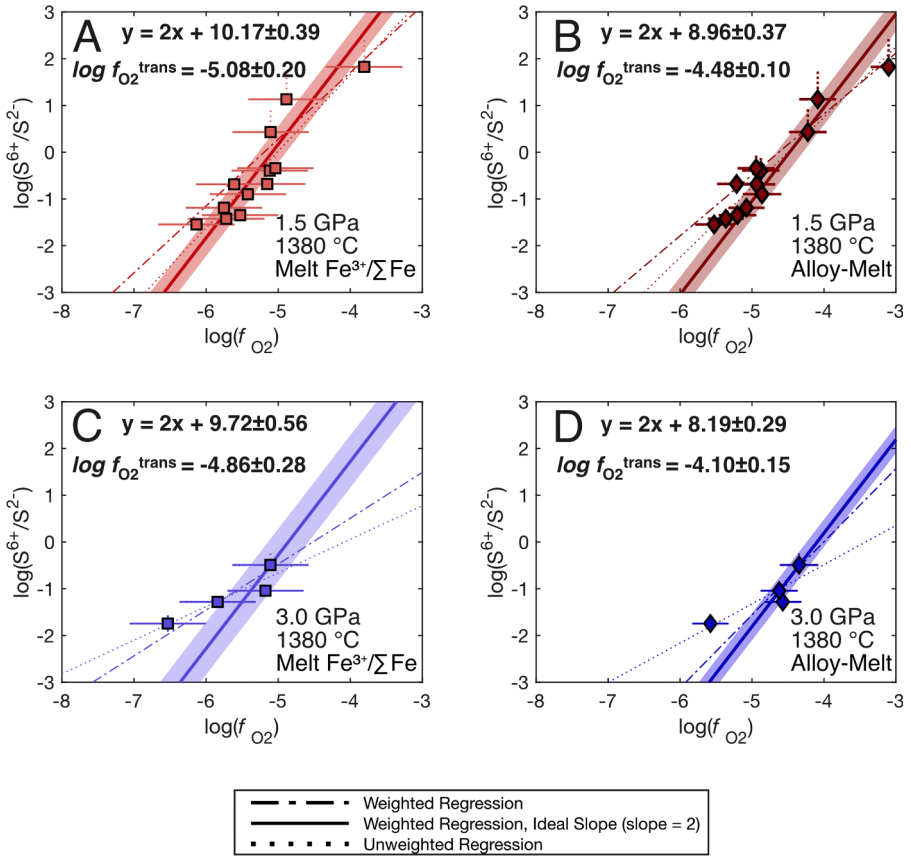

Fig. 4. The experimental data, as in Fig. 3, recast in terms of $\log(S^{6+}/S^{2-})$. Lines are regressions through data at each pressure and with each experiment f_{O2} calculation method. The dotted lines are an unweighted linear regression. Dashed lines are a weighted linear regression using the uncertainty of $\log(S^{6+}/S^{2-})$ values. Solid lines are a weighted linear regression forced to a calculated slope from thermodynamic considerations (slope ≡ 2; Jugo et al. 2010). The shaded region for this regression is the 95 % confidence interval. We use the weighted regression with the ideal slope as the basis for our models and discussion. Equations shows the weighted, forced slope regression equation of each fit.

2017; Muth and Wallace 2021; Jugo et al. 2010; Botcharnikov et al. 2011, O'Neill and Mavrogenes 2022, Boulliung and Wood 2023). To quantify this relationship, we performed three different regressions of $\log(S^{6+}/S^{2-})$ as a function of $\log f_{O2}$. The first is an unweighted linear regression. The second is a weighted linear regression. We use a weighted regression because the reproducibility of $\log(S^{6+}/S^{2-})$ values from S-XANES analyses decreases with increasing values of $\log(S^{6+}/S^{2-})$ and hence lower concentrations of S^{2-}. To account for this, in our second regression, we weight each data point by the inverse of the measurement uncertainty in $\log(S^{6+}/S^{2-})$. The third regression is weighted in the same way and slope is fixed equal to 2, which is the slope predicted by thermodynamic calculations and reproduced experimentally in prior studies (Jugo et al. 2010).

In the 1.5 GPa series, all three regression approaches yield similar results. The 1.5 GPa series is better constrained because it contains a broader range of $S^{6+}/\Sigma S$ values (0.03 to 0.99). In the 3 GPa series, where all experiments are sulfate-poor, and the fit is less well-constrained, the results of these three regressions diverge. Although the 3 GPa series has fewer experiments, none of the experiments have an outsized influence on regressions (Supp. Fig. 6). Because the 1.5 GPa series is in good agreement with the theoretical slope and consistent with previous studies, we favor the regression with slope ≡ 2. This regression fits experimental data at both pressures within uncertainty except for experiments with high and low values of melt $S^{6+}/\Sigma S$. For example, the lowest and highest $\log(S^{6+}/S^{2-})$ experiments plotted in Fig. 4 have melt $S^{6+}/\Sigma S$ values of 0.03 and 0.99, respectively. It may be that we underpredict measurement uncertainty in these glasses.

The relationship between $S^{6+}/\Sigma S$ and absolute f_{O2} does not differ strongly between the 1.5 and 3 GPa series. In data calculated using melt $Fe^{3+}/\Sigma Fe$ equilibria, $\log f_{O2}^{trans}$ is shifted to higher f_{O2} by 0.22±0.34 log units as pressure increases from 1.5 to 3 GPa,. In data calculated using melt-alloy equilibria, $\log f_{O2}^{trans}$ shifts up from 1.5 to 3 GPa by 0.38±0.18 log units. Uncertainty for these values is calculated using the 95 % regression confidence interval of the x-axis intercept, which is constant due to the fixed slope of the regression. The mean of these two results to yields a pressure dependence for absolute $\log f_{O2}^{trans}$ of 0.20±0.13/GPa, where the uncertainty is the propagated uncertainty on the values from each method as listed above.

4. Discussion

4.1. Comparison to previous models and choice of reference buffer

Fig. 5 compares our data to model calculations of Boulliung and Wood (2023), hereafter BW23. BW23 calculations are based on an experimentally calibrated thermodynamic model of sulfur speciation as a function of f_{O2} at one atmosphere. In addition to this calibrated model, BW23 additionally calculates a pressure effect based on the molar volumes of solid FeS, FeO, $CaSO_4$, and CaO crystalline compounds. Crystalline compounds are used because partial molar volume data is not available for FeS and $CaSO_4$ as components in silicate melt. The BW23 calculations suggest that the effect of pressure on sulfur speciation as a function of absolute f_{O2} is small, and favors S^{6+} at high pressure, which is consistent with our results (Fig. 2). At 1380 °C (the temperature of our experiments), this model predicts that from 1.5 to 3 GPa, absolute $\log(f_{O2}^{trans})$ is shifted upward by 0.54 log units, which is broadly consistent with our results.

Absolute f_{O2} of melts does not stay constant in natural systems, because f_{O2} depends on pressure and temperature even if the bulk chemical composition of a given system remains constant. During closed system adiabatic decompression, the absolute f_{O2} of a basaltic melt changes and these changes roughly parallel the QFM buffer (Kress and Carmichael, 1991). However, at low melt fractions, melts decompress in equilibrium with their ultramafic host rock until some pressure of melt segregation to dunite conduits (Kelemen et al., 1995). Thus, while basaltic melts roughly parallel the QFM buffer during decompression (Kress and Carmichael, 1991), the same is not true of a decompressing melt-peridotite system. The absolute $\log f_{O2}$ of the Ferrosilite-Fayalite-Magnetite (FFM) buffer (eqn. 4 of Davis et al., 2017) is more likely to parallel decompressing spinel peridotite (±melt) because the minerals in this buffer assemblage are similar to a spinel peridotite mineral assemblage (Stolper, 2020; Birner et al., 2024). The

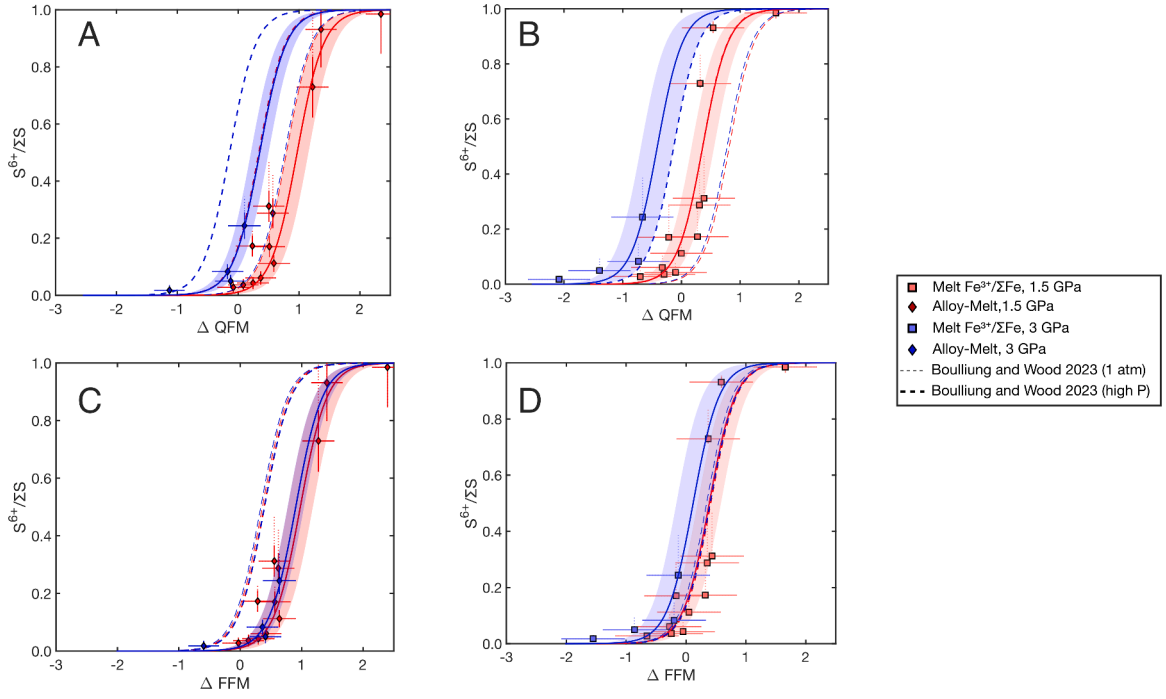

Fig. 5. Experimental data, where f_{O2} is re-plotted relative to the QFM buffer (panels A and B; Frost 1991) and the FFM buffer (panels C and D; Davis et al., 2017). Solid lines (from Fig. 3) are regressions of the experimental data, and shaded regions indicate each regression's 95 % confidence interval. Thin and thick dashed lines show the 1 atm and high-pressure (1.5 and 3.0 GPa) thermodynamic models, respectively, of Boulliung and Wood (2023).

log f_{O2} of peridotites does change over the pressure range of mantle melting, although f_{O2} relative to FFM should remain very stable over the spinel peridotite melting interval (Stolper, 2020; Birner et al., 2024). There is also good observational and experimental data to support models in which relative f_{O2} remains constant as melting proceeds (Davis and Cottrell 2018; Sorbadere et al. 2018; Birner et al. 2021; Moussallam et al., 2023).

When melts segregate from mantle peridotite, they can be approximated as systems closed to oxygen. In S-free melts, where Fe is the only major element with multiple valence states, melt $Fe^{3+}/\Sigma Fe$ stays constant and the change in absolute f_{O2} can be calculated using formulations of $Fe^{3+}/\Sigma Fe$ as a function of f_{O2} based on experimental data (e.g., Kress and Carmichael 1991; O'Neill et al., 2006; Zhang et al., 2017). This is the f_{O2} change that is approximately parallel to that of the QFM buffer. However, in S-bearing systems, S and Fe may undergo redox exchange, which would change the melt $Fe^{3+}/\Sigma Fe$ and $S^{6+}/\Sigma S$.

As a simple first step toward applying our results to natural systems, we recast both BW23 and our experimental data relative to QFM and FFM. We use both buffers because each buffer has a different pressure dependence. In data calculated using melt-alloy equilibria, from 1.5 to 3 GPa log $f_{O2}^{tr\_ans}$ shifts by -0.62 ± 0.18 relative to QFM . In data calculated using melt $Fe^{3+}/\Sigma Fe$ equilibria, from 1.5 to 3 GPa log $f_{O2}^{tr\_ans}$ shifts by -0.78 ± 0.34 relative to QFM. Taking the mean of these two values yields a pressure dependence for log f_{O2}^{trans} of -0.47 ± 0.08/GPa relative to the QFM buffer. BW23 predicts that at the temperature of our experiments (1380 °C) log f_{O2}^{trans} is shifted by -0.30/GPa relative to QFM. The overall agreement between our experimental results and the model of BW23 supports the BW23 model. While the temperature effect of BW23 is constrained with experimental data, the pressure effect of BW23 is a very simplified estimate based on the molar volumes of solid end-member compounds. Our experimental results suggest that even this simplified approach can reproduce both the direction and magnitude of the effect of pressure on melt $S^{6+}/\Sigma S$.

When we cast our data using melt-alloy equilibria relative to FFM, the effect of pressure from 1.5 to 3 GPa is very small and is not statistically significant. From 1.5 to 3 GPa log $f_{O2}^{tr\_ans}$ shifts by -0.09 ± 0.12 log units relative to FFM. When we use melt $Fe^{3+}/\Sigma Fe$ equilibria, from 1.5 to 3 GPa, log f_{O2}^{trans} shifts by -0.20 ± 0.23 log units relative to FFM. Taking the average of these two values yields a pressure dependence for log f_{O2}^{trans} of -0.14 ± 0.13/GPa relative to FFM. BW23 predicts that at the temperature of our experiments (1380 °C) log f_{O2}^{trans} is shifted by 0.02/GPa relative to FFM. The lack of pressure effect relative to the FFM buffer is likely a coincidence, as there is no clear reason why the molar volumes of the melt components relevant to S redox reactions (e.g., FeS, $CaSO_4$, etc.) would correspond to the molar volumes of the components of the FFM buffer (Fayalite, Ferrosilite, and Magnetite). That being said, the implications of this similarity for natural systems are significant, as detailed in the following sections.

Our results contrast with the experiments of Matjuschkin et al. (2016), which indicated that absolute $f_{O2}^{tr\_ans}$ increases with increasing pressure. Some of the differences between the pressure effect inferred from the experiments of Matjuschkin et al. (2016) and our own results are due to the choice of the buffer system. The results of Matjuschkin et al. (2016) are expressed relative to the Nickel-Nickel-Oxide (NNO) buffer which has a different pressure dependence compared to QFM or FFM. Matjuschkin et al. (2016) report that the melt anhydrite stability field increases from roughly $\Delta NNO = 2$ to $\Delta NNO = 3$ from 0.5 to 1 GPa. At the temperature range of their experiments (850–950 °C) and over the same pressure interval, this is equivalent to a shift from $\Delta QFM = 2.8$ to $\Delta QFM = 3.2$. Even with this consideration, however, our results still predict a shift in a direction opposite to that of Matjuschkin et al. (2016). The experiments of Matjuschkin et al. (2016) differ from our own in that they use buffer systems to estimate experiment f_{O2} instead of measuring experiment f_{O2} using melt $Fe^{3+}/\Sigma Fe$ or melt-alloy equilibria, and they also infer melt $S^{6+}/\Sigma S$ from melt sulfur concentrations instead of measuring melt $S^{6+}/\Sigma S$ via XANES as we have in this study. The experiments of Matjuschkin et al. (2016) were conducted using a trachyandesite composition, did not include any experiments above 1.5 GPa, and contained an H_2O-rich vapor phase. Due to these differences in experimental design and analytical methodology, it is not easy to identify why the results of Matjuschkin et al. (2016) diverge from our own.

4.2. Application to mantle melts in natural settings

To apply our results to mantle melting we consider two end-member scenarios of melt f_{O2} evolution. In one scenario, melt is in equilibrium with mantle peridotite. Melt S and Fe valence state will therefore be controlled by the f_{O2} imposed by the mantle peridotite mineral assemblage. In the second scenario, the melt is isolated, and S and Fe valence state are controlled by equilibrium electron exchange reactions.

In natural systems, the melts that erupt have experienced some complex middle ground between these two end-member scenarios. Beneath mid-ocean ridges, melts initially form in equilibrium with the mantle but are aggregated and transported through dunite channels that are more chemically inert than peridotite prior to eruption (Kelemen et al. 1995). Transport mechanics beneath volcanic arcs are less well-constrained. However, melt thermobarometry suggests that most arc melts remain in equilibrium with mantle peridotite until ~1–1.5 GPa (Till 2017).

To assess how melt $S^{6+}/\Sigma S$ varies with pressure in natural systems, we create a simplified two-stage model using both end-member scenarios. We assume that from 2 to 1 GPa, melts remain in equilibrium with the surrounding mantle peridotite, and from 1 GPa to the surface the melt is a closed system. This is intended to approximate the transition from melts in equilibrium with mantle peridotite to chemically isolated melts ascending to the surface.

We create three sets of calculations using this model. The first approximates melting underneath mid-ocean ridges. We begin the calculation by assuming a representative MORB melt composition (primary MORB AII; Cottrell and Kelley 2011) with 1000 ppm S (similar to concentrations measured in primitive MORB; Jenner et al., 2012), $Fe^{3+}/\Sigma Fe = 0.14$ and $S^{6+}/\Sigma S = 0.05$ (similar to values measured in MORB; Zhang et al., 2018, Muth and Cottrell 2023, Lerner et al., 2021). These assumptions constrain the major element composition and redox budget of the melt.

To calculate the closed system part of our two-stage model, we apply the model of Kress and Carmichael (1991) to calculate S-Fe redox exchange along a melt adiabat, starting at 1 GPa and 1358 °C and ending at 0.1 GPa and 1343 °C. We chose the initial temperature to be consistent with a mantle potential temperature of 1350 °C in the deeper (1–2 GPa) section of the model. Because the equation of Kress and Carmichael (1991), like other formulations of f_{O2} as a function of melt $Fe^{3+}/\Sigma Fe$, is not stoichiometric, we used a non-stoichiometric S-Fe reaction equation to calculate this exchange. We use f_{O2} relative to FFM (i.e., ΔFFM; Davis et al., 2017), at 1 GPa during the first stage of the calculation as the f_{O2} for first step of the second stage of the calculation. We then use this ΔFFM value as an initial condition to calculate equilibrium $Fe^{3+}/\Sigma Fe$ and $S^{6+}/\Sigma S$ along a prescribed P-T path taken from the adiabatic decompression melting model of Birner et al. (2024) at a mantle potential temperature of 1350 °C. The MATLAB script used for these calculations is in the Supplementary Material and a more detailed model description is found in the Supplementary Text.

The second two calculations approximate melting beneath volcanic arcs. We conduct calculations along the same P-T paths as described above but make two changes to our initial assumptions. In the first model (red lines in Fig. 7), we change the melt sulfur concentration from 1000 ppm to 2500 ppm S (representative arc basalt concentration; Muth and Wallace 2022). In the second model (blue lines in Fig. 7) we keep the assumption of 2500 ppm S and also change the assumed Fe and S valence state to match typical values measured at volcanic arcs (Cottrell et al., 2021; Muth and Wallace, 2021).

In all models, melt $S^{6+}/\Sigma S$ stays relatively constant throughout mantle melting and ascent, even in S^{6+}- rich basalts. This constant melt $S^{6+}/\Sigma S$ occurs because as melt S-Fe redox equilibria shifts with pressure (this occurs in both stages of the model; Supp. Fig. 12), and as the melt gains or loses electrons as it equilibrates with mantle peridotite (this occurs in the 2→1 GPa stage of the model, where the melt is decompressing in equilibrium with peridotite), chemical changes are accommodated primarily by the oxidation or reduction of Fe, allowing melt $S^{6+}/\Sigma S$ to stay relatively constant. While this may seem surprising given the higher concentration of Fe relative to S in basaltic melts, it is important to keep in mind that oxidation or reduction of S in silicate melt requires eight electrons, while oxidation or reduction of Fe only requires one. A melt decompressing along a line of constant melt $S^{6+}/\Sigma S$ evolves in f_{O2} roughly parallel to the FFM buffer (~0.38 log units/GPa), whereas the pressure dependence of the QFM buffer is a factor of two larger.

4.3. Implications for natural data sets

Our experimental results reinforce long-standing interpretations of sulfur behavior during mantle melting beneath mid-ocean ridges. The current paradigm is that under mid ocean ridges, most melting takes place under sulfide-saturated conditions (Mathez, 1976). However, because sulfide content at sulfide saturation (S^{2-}CSS) increases with decreasing pressure, models predict that melts will arrive in the crust slightly sulfide undersaturated (Mavrogenes and O'Neill 1999; Holzheid and Grove 2002). As the melts begin to cool, S^{2-}CSS decreases, and the melts quickly become sulfide saturated. This paradigm is supported by S^{2-}CSS models (Mavrogenes and O'Neill 1999; Holzheid and Grove 2002; O'Neill 2021), and observations of sulfur and chalcophile element behavior (Mathez 1976; Peach et al., 1990; Czamanske and Moore 1977). We now know that MORB glasses have low but measurable $S^{6+}/\Sigma S$ (Lerner et al., 2021; Muth and Cottrell 2023). If melt $S^{6+}/\Sigma S$ were to strongly increase with pressure, we would predict high melt sulfur concentrations ($SCSS^T$ i.e., S^{2-}CSS plus the additional contribution of melt S^{6+}) and rapid exhaustion of sulfide during mantle melting. This would mean the stability of sulfides during mantle melting would vary more strongly with depth than S^{2-}CSS models alone account for. Instead, our results show that the low $S^{6+}/\Sigma S$ measured in MORB glasses reflects low melt $S^{6+}/\Sigma S$ in the MORB-source mantle, and petrologic interpretations based on S^{2-}CSS models are still applicable, albeit with a small but relatively constant contribution of S^{6+} to $SCSS^T$.

Our results allow us to model sulfur behavior at volcanic arcs with greater confidence than was possible previously. Arc basalts have high $S^{6+}/\Sigma S$ compared to MORB (Rowe et al., 2009; Muth and Wallace 2021; Muth and Wallace 2022). Because $SCSS^T$ increases exponentially with $S^{6+}/\Sigma S$, in arc basalts changes in $SCSS^T$ are much larger for a given change in $S^{6+}/\Sigma S$ compared to MORB. Therefore, uncertainty about the relationship between f_{O2} and basaltic melt $S^{6+}/\Sigma S$ at mantle pressures has made it extremely difficult to model sulfur and chalcophile element behavior during mantle melting. Our results demonstrate that $S^{6+}/\Sigma S$ in arc basalts does not vary strongly during mantle melting and ascent (Fig. 7). If melt $S^{6+}/\Sigma S$ remains stable, $SCSS^T$ will respond to pressure and temperature in a way that is roughly parallel to the response of S^{2-}CSS. Therefore, it is probable that, like MORB, many arc basalts are sulfide-saturated during mantle melting, then arrive at the crust slightly sulfide-undersaturated. This prediction is consistent with observed similarities between the copper content of MORB and arc basalts (Lee et al., 2012; Muth and Wallace 2022), and early crystallization of sulfide phases often observed in arc magmas (e.g., Georgatou et al., 2018; Cox et al., 2019).

Some back-arc and tholeiitic arc basalts depart from the overall trend of early sulfide-saturation and are sulfide-undersaturated (Lee et al., 2012; Jenner et al., 2015). Previous authors have explored whether the depth of crystallization can explain differences in the timing of sulfide saturation between magmas in continental arcs and magmas in oceanic arcs (e.g., Rezeau and Jagoutz 2020). In this conceptual model, melts at continental arcs crystallizing at higher pressure have lower melt $S^{6+}/\Sigma S$ and therefore lower $SCSS^T$ relative to melts at oceanic arcs crystallizing at lower pressure. Our results are not consistent with this model because we do not find evidence that melt $S^{6+}/\Sigma S$ changes with pressure in arc basalts, although we cannot exclude the possibility that our results are not applicable to more evolved melts like the trachyandesites studied by Matjuschkin et al. (2016).

As in previous modeling efforts (Muth and Wallace 2021), the results of these calculations demonstrate the importance of S-Fe electron exchange in S^{6+}-rich melts. Calculations that do not incorporate S-Fe electron exchange would predict constant melt $Fe^{3+}/\Sigma Fe$ during closed system melt ascent in arc magmas. In contrast, due to shifting equilibrium S-Fe exchange with pressure and temperature, our calculations predict a slight increase in melt $Fe^{3+}/\Sigma Fe$ systematically with ascent (decreasing pressure; Figs. 6, 7). This increase means that melt $Fe^{3+}/\Sigma Fe$ measured in erupted basalts is slightly higher than the basalts last in equilibrium with the mantle. This effect is likely negligible in mid-ocean ridge settings, where basalts have very low $S^{6+}/\Sigma S$ and relatively low S concentrations. In volcanic arcs, this effect is modest but may be non-negligible. For example, the 'high S, high $S^{6+}/\Sigma S$' model in Fig. 7 (red curve) predicts that a melt with $Fe^{3+}/\Sigma Fe = 0.2$ and $S^{6+}/\Sigma S = 0.7$ at the surface would have a log f_{O2} of $\Delta QFM = 0.7$ at 1 GPa. In contrast, a model that did not account for S-Fe redox exchange and instead assumed melt $Fe^{3+}/\Sigma Fe$ stays constant would predict the melt would have a log f_{O2} of $\Delta QFM = 0.9$ at 1 GPa. The magnitude of uncertainty associated with S-Fe redox exchange will vary depending on melt composition, so we encourage authors to use our code supplied in the Supplementary Material for their compositions of interest.

For S^{6+}-rich terrestrial arc basalts with modest FeO^T concentrations, S dominates the electron exchange. In our models of S^{6+}-rich arc basalts (Fig. 7), melt $S^{6+}/\Sigma S$ stays constant and melt f_{O2} is parallel to the FFM buffer during mantle melting and melt ascent. We therefore suggest that for some S^{6+}-rich melts, FFM can be a more appropriate reference buffer for the f_{O2} of closed-system ascending basalts than QFM.

Our results show that S^{6+}measured in erupted basalts is representative of S^{6+} present during mantle melting conditions. This means that mantle melting calculations may also need to take the presence of S^{6+} into account even under relatively reducing conditions such as at mid-ocean ridge spreading centers. That said, we caution that our calculations are simplified and intended to provide first-order constraints for the implications of our experiments. Modeling efforts with a more sophisticated treatment of f_{O2} during mantle melting and melt extraction could elucidate to what extent the presence of S^{6+} influences inferred mantle f_{O2}.

5. Conclusions

We conducted a series of experiments at 1.5 and 3 GPa with variable f_{O2}. For each experiment, we measured experiment melt f_{O2} using both basalt Fe-XANES and alloy-melt equilibria and measured melt $S^{6+}/\Sigma S$ using S-XANES. We compared results from each series to quantify the effect of pressure on the relationship between melt f_{O2} and $S^{6+}/\Sigma S$. When we calculate our results using absolute f_{O2}, we calculate an empirical pressure dependence for absolute log $f_{O2}^{tr\_ans}$ of 0.20±0.13/GPa. We calculate an empirical pressure dependence for log $f_{O2}^{tr\_ans}$ of −0.47±0.13/GPa relative to QFM, and −0.14±0.13/GPa relative to FFM.

To calculate how melt $S^{6+}/\Sigma S$ changes during mantle melting and melt ascent, we construct a S-Fe redox exchange model based on previous thermodynamic calculations and find that melt $S^{6+}/\Sigma S$ does not strongly change during mantle melting and closed system melt ascent. This indicates that melt $S^{6+}/\Sigma S$ measured in primitive, undegassed melts at the surface is broadly representative of melt $S^{6+}/\Sigma S$ in their high-pressure source regions. Even mantle melts in relatively reduced settings like those beneath mid-ocean ridges may contain a non-negligible

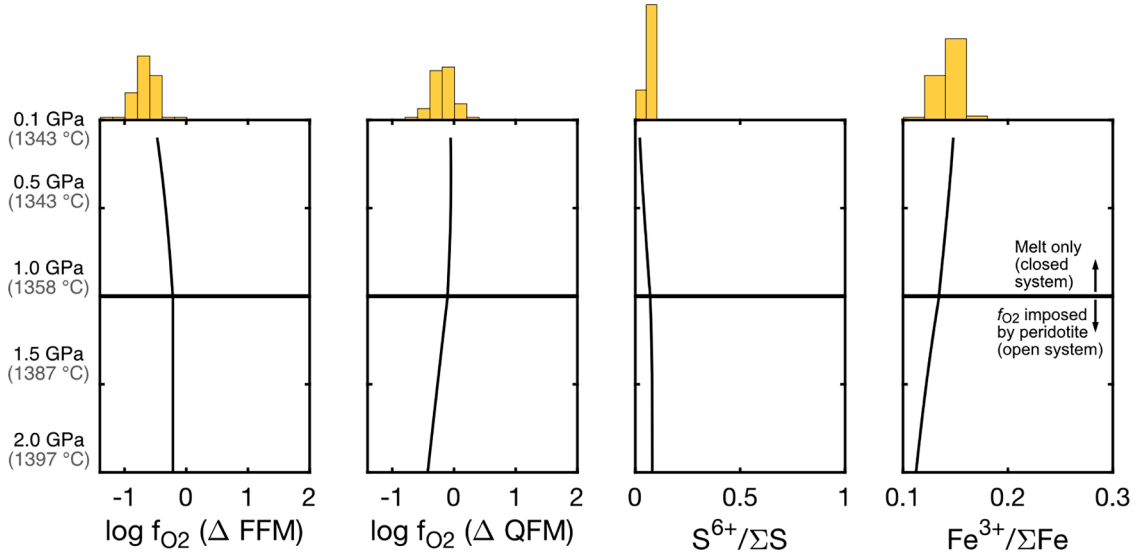

Fig. 6. Simplified calculation of melt S and Fe valence state underneath mid-ocean ridges. From 2 to 1 GPa, we approximate a melt in f_{O2} equilibrium with a mantle peridotite by maintaining a constant ΔFFM. From 1 to 0.1 GPa, we approximate chemically isolated ascending melts by calculating S-Fe exchange in an adiabatically ascending melt closed to f_{O2}. Melt composition is a calculated primary MORB with 1000 ppm S, $Fe^{3+}/\Sigma Fe = 0.14$, and $S^{6+}/\Sigma S = 0.05$. The histograms show calculated f_{O2} ($n = 103$), measured $S^{6+}/\Sigma S$ ($n = 5$), and measured $Fe^{3+}/\Sigma Fe$ ($n = 103$) values in natural MORB glasses with both S and Fe valence state determinations (Cottrell et al., 2021; Lerner et al., 2021; Muth and Cottrell, 2023).

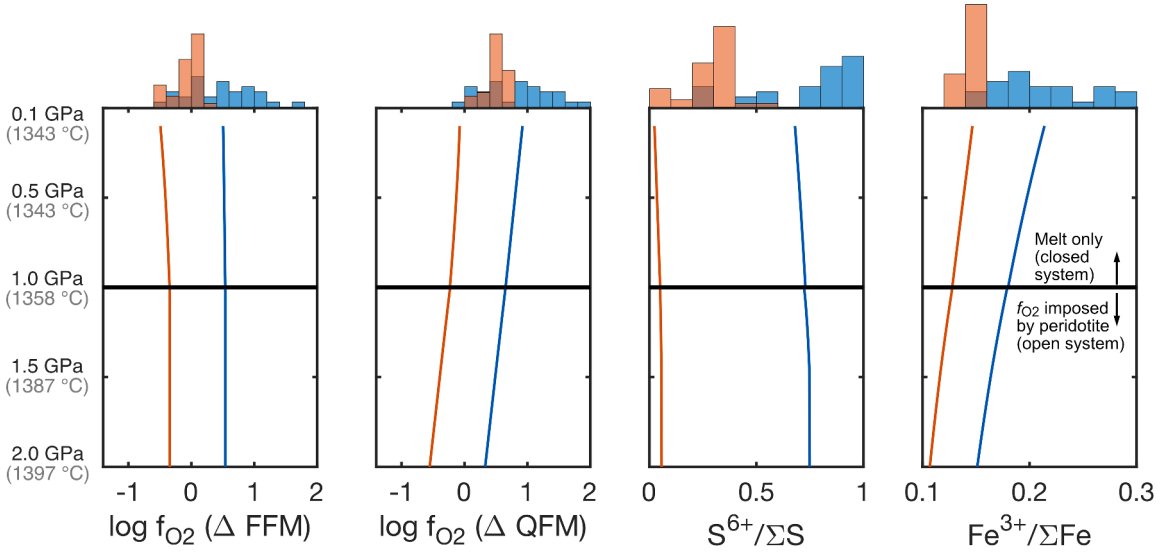

Fig. 7. Simplified calculation of melt S and Fe valence state underneath volcanic arcs. The calculation approach is the same as that used in Fig. 6. The red model melt composition is a calculated primary basalt with 2500 ppm S, $Fe^{3+}/\Sigma Fe = 0.14$ and $S^{6+}/\Sigma S = 0.05$. Blue model melt composition is a calculated primary basalt with 2500 ppm S, $Fe^{3+}/\Sigma Fe = 0.20$, and $S^{6+}/\Sigma S = 0.70$. The histograms show calculated f_{O2}, measured $S^{6+}/\Sigma S$ and measured $Fe^{3+}/\Sigma Fe$ values in natural subduction zone glasses with both S and Fe valence state determinations. Blue data are melt inclusions from the Cascades Arc ($n = 31$; Muth et al., 2021) and volcanic glasses from the Troodos Ophiolite ($n = 37$; Saper et al. 2024b).

amount of S^{6+}, although more detailed analyses and modelling would be needed to confirm this.

Our experimental results and models reinforce the currently held conceptual models for sulfur behavior during melting beneath mid-ocean ridges. They also dramatically improve the accuracy of modeled sulfur behavior during mantle melting beneath volcanic arcs. We suggest that many arc magmas follow patterns of sulfide saturation similar to that of MORB and that differences in storage pressure alone cannot explain differences in sulfide saturation behavior between continental and oceanic arcs. Finally, we emphasize the importance of considering S-Fe electron exchange reactions within models of mantle melting and early crystallization in S^{6+}- rich magmas and demonstrate that failing to account for these reactions can lead to a small but non-negligible overestimate of mantle source f_{O2} for volcanic arc basalts.

CRediT authorship contribution statement

Michelle J. Muth: Writing – review & editing, Writing – original draft, Visualization, Methodology, Investigation, Funding acquisition, Formal analysis, Data curation. **Elizabeth Cottrell:** Writing – review & editing, Methodology, Investigation, Funding acquisition, Conceptualization.

Declaration of competing interest

The authors declare that they have no known competing financial interests or personal relationships that could have appeared to influence the work reported in this paper.

Acknowledgments

We thank Fred Davis for many useful discussions regarding experimental design and for implementation of the Hirschman and Zhang (2023) Pt-Fe solution model. We thank Tony Lanzirotti and Matt Newville for their assistance at the Advanced Photon Source and Ryan Tappero for their assistance at the National Synchrotron Light Source II. We thank Tim Gooding for discussions and assistance with capsule machining. We thank Dante Canil, Marc Hirschmann, and Lee Saper for helpful discussions. We acknowledge the support of GeoSoilEnviroCARS (The University of Chicago, Sector 13), which is supported by the National Science Foundation—Earth Sciences (EAR—1634415) and Department of Energy- GeoSciences (DE-FG02–94ER14466). This research used resources from the Advanced Photon Source, a U.S. Department of Energy (DOE) Office of Science User Facility operated for the DOE Office of Science by Argonne National Laboratory under Contract No DE-AC02–06CH1135. This research used resources of the National Synchrotron Light Source-II XFM beamline operated for the DOE Office of Science by Brookhaven National Laboratory under Contract No DE-SC0012704. Experimental consumables were supported by a Smithsonian Scholarly Studies grant to E.C. This study was made possible by a Smithsonian Peter Buck Fellowship to M.M.

Supplementary materials

Supplementary material associated with this article can be found, in the online version, at doi:10.1016/j.epsl.2025.119562.

Data availability

Data is included in the supplemental material

References

Andrys, J.L., Cottrell, E., Kelley, K.A., Waters, L.E., Coombs, M.L., 2024. Insights on arc magmatic systems drawn from natural melt inclusions and crystallization experiments at P_{H2O} = 800 MPa under oxidizing conditions. J. Petrol. 65.

Birner, S.K., Cottrell, E., Warren, J.M., Kelley, K.A., Davis, F.A., 2021. Melt addition to mid-ocean ridge peridotites increases spinel Cr# with no significant effect on recorded oxygen fugacity. Earth Planet. Sci. Lett 566.

Birner, S.K., Cottrell, E., Davis, F.A., Warren, J.M., 2024. Deep, hot, ancient melting recorded by ultralow oxygen fugacity in peridotites. Nature 631, 801–807.

Borisov, A., Behrens, H., Holtz, F., 2018. Ferric/ferrous ratio in silicate melts: a new model for 1 atm data with special emphasis on the effects of melt composition. Contrib. Mineral. Petrol. 173–198.

Botcharnikov, R.E., Linnen, R.L., Wilke, M., et al., 2011. High gold concentrations in sulphide-bearing magma under oxidizing conditions. Nat Geosci 4, 112–115. https://doi.org/10.1038/ngeo1042.

Boulliung, J., Wood, B.J., 2023. Sulfur oxidation state and solubility in silicate melts. Contrib Miner. Pet. 178, 1–15. https://doi.org/10.1007/s00410-023-02033-9.

Brooker, R.A., Holloway, J.R., Hervig, R., 1998. Reduction in piston-cylinder experiments: the detection of carbon infiltration into platinum capsules. Am. Mineral. 83, 985–994.

Brounce, M., Stolper, E., Eiler, J., 2017. Redox variations in Mauna Kea lavas, the oxygen fugacity of the Hawaiian plume, and the role of volcanic gases in Earth's oxygenation. Proc Natl Acad Sci U S A 114, 8997–9002.

Carmichael, I.S.E., Ghiorso, M.S., 1986. Oxidation-reduction relations in basic magma: a case for homogenous equilibria. Earth Planet. Sci. Lett 78, 200–210.

Carroll, M.R., Rutherford, M.J., 1988. Sulfur speciation in hydrous experimental glasses of varying oxidation state: results from measured wavelength shifts of sulfur X-rays. Am. Mineral. 73, 845–849.

Christien, F., 2020. Role of impurity sulphur in the ductility trough of austenitic iron-nickel alloys. Mater. (Basel) 13, 1–8. https://doi.org/10.3390/ma13030539.

Czamanske, G.K., Moore, J.G., 1977. Composition and phase chemistry of sulfide globules in basalt from the Mid-Atlantic Ridge rift valley near 37°N. Geol Soc Am Bull 88 (587–599), 33–61. https://doi.org/10.1002/9781119473206.ch3.

Cottrell, E., Kelley, K.A., 2011. The oxidation state of Fe in MORB glasses and the oxygen fugacity of the upper mantle. Earth Planet. Sci. Lett 305, 270–282.

Cottrell, E., Birner, S.K., Brounce, M., Davis, F.A., Waters, L.E., Kelley, K.A., 2021. Oxygen fugacity across tectonic settings. Magma Redox Geochem.

Cox, D., Watt, S.F.L., Jenner, F.E., Hastie, A.R., Hammond, S.J., 2019. Chalcophile element processing beneath a continental arc stratovolcano. Earth Planet. Sci. Lett 522, 1–11.

Davis, F.A., Cottrell, E., Birner, S.K., Warren, J.M., Lopez, O.G., 2017. Revisiting the electron microprobe method of spinel-olivine-orthopyroxene oxybarometry applied to spinel peridotites. Am. Mineral. 102 (2), 421–435.

Davis, F.A., Cottrell, E., 2018. Experimental investigation of basalt and peridotite oxybarometers: implications for spinel thermodynamic models and Fe^{3+} compatibility during generation of upper mantle melts. Am. Mineral. 103, 1056–1067.

Davis, F.A., Cottrell, E., 2021. Partitioning of Fe_2O_3 in peridotite partial melting experiments over a range of oxygen fugacities elucidates ferric iron systematics in mid-ocean ridge basalts and ferric iron content of the upper mantle. Contrib. Mineral. Petrol. 176. https://doi.org/10.1007/s00410-021-01823-3.

Ding, S., Plank, T., Wallace, P.J., Rasmussen, D.J., 2023. Sulfur_X: a model of sulfur degassing during Magma ascent. Geochem. Geophys. Geosystems 24.

Evans, K.A., 2012. The redox budget of subduction zones. Earth-Sci. Rev. 113, 11–32.

Frost, B., 1991. Introduction to oxygen fugacity and its petrologic importance. Rev. Mineral. Geochem. 25, 1–10.

Gaetani, G.A., Grove, T., 1998. The influence of water on melting of mantle peridotite. Contrib. Mineral. Petrol. 131, 323–346.

Georgatou, A., Chiaradia, M., Rezeau, H., Wälle, M., 2018. Magmatic sulphides in quaternary ecuadorian arc magmas. Lithos 296-299, 580–599.

Hirschmann, M.M., Zhang, H.L., 2023. A revised model for activity-compositon relations in solid and molten FePt alloys and a preliminary model for characterization of oxygen fugacity in high pressure experiments. Eur. J. Mineral. 993–1001. https://doi.org/10.5194/ejm-35-789-2023.

Holzheid, A., Grove, T.L., 2002. Sulfur saturation limits in silicate melts and their implications for core formation scenarios for terrestrial planets. Am. Mineral. 87, 227–237.

Hughes, E.C., Saper, L.M., Liggins, P., O'Neill, H.S.C., Stolper, E.M., 2023. The sulfur solubility minimum and maximum in silicate melt. J Geol Soc Lond. 180.

Jenner, F.E., O'Neill, H.S.C., 2012. Analysis of 60 elements in 616 ocean floor basaltic glasses. Geochem. Geophys. Geosystems 13.

Jenner, F.E., Hauri, E.H., Bullock, E.S., König, S., Arculus, R.J., Mavrogenes, J.A., Mikkelson, N., Goddard, C., 2015. The competing effects of sulfide saturation versus degassing on the behavior of the chalcophile elements during the differentiation of hydrous melts. Geochem. Geophys. Geosystems 16, 1490–1507.

Jugo, P.J., Wilke, M., Botcharnikov, R.E., 2010. Sulfur K-edge XANES analysis of natural and synthetic basaltic glasses: implications for S speciation and S content as function of oxygen fugacity. Geochim. Cosmochima Acta 74, 5926–5938. https://doi.org/10.1016/j.gca.2010.07.022.

Kelemen, P.B., Shimizu, N., Salters, V.J.M., 1995. Extraction of mid-ocean ridge basalt from the upwelling mantle by focused flow melt in dunite channels. Nature 375, 747–753.

Kessel, R., Beckett, J.R., Stolper, E.M., 2001. Thermodynamic properties of the Pt-Fe system. Am. Mineral. 86, 1003–1014.

Kress, V.C., Carmichael, I.S.E., 1991. The compressibility of silicate liquids containing Fe_2O_3 and the effect of composition, temperature, oxygen fugacity and pressure on their redox states. Contrib. Mineral. Petrol. 108, 82–92.

Lee, C.T., Luffi, P., Chin, E.J., Bouchet, R., Dasgupta, R., Morton, D.M., Le Roux, V., Yin, Q.Z., Jin, D., 2012. Copper systematics in arc magmas and implications for crust-mantle differentiation. Science 336, 64–68.

Lerner, A.H., Muth, M.J., Wallace, P.J., Lanzirotti, A., Newville, M., Gaetani, G.A., Chowdhury, P., Dasgupta, R., 2021. Improving the reliability of Fe- and S-XANES measurements in silicate glasses: correcting beam damage and identifying Fe-oxide nanolites in hydrous and anhydrous melt inclusions. Chem, Geol 586 (October), 120610. https://doi.org/10.1016/j.chemgeo.2021.120610.

Liu, X.I., O'Neill, H.S.C., Berry, A.J., 2006. The effects of small amounts of H_2O, CO_2 and Na_2O on the partial melting of spinel lherzolite in the system CaO–MgO–Al_2O_3–SiO_2 ± H_2O ± CO_2 ± Na_2O at 1.1 GPa. J. Petrol. 47, 409–434.

Luhr, J.F., Carmichael, I.S.E., Varekamp, J.C., 1984. The 1982 eruptions of El Chichón Volcano, Chiapas, Mexico: mineraology and petrology of the anhydrite-bearing pumices. J. Volcanol. Geotherm. Res. 23, 69–108.

Luhr, J.F., 1990. Experimental phase relations of water- and sulfur- saturated arc magmas and the 1982 eruptions of El Chichón Volcano. J. Petrol. 31, 1071–1114.

Mathez, E.A., 1976. Sulfur solubility and magmatic sulfides in submarine basalt glass. J. Geophys, Res 81, 4269–4276.

Matjuschkin, V., Blundy, J.D., Brooker, R.A., 2016. The effect of pressure on sulphur speciation in mid- to deep-crustal arc magmas and implications for the formation of porphyry copper deposits. Contrib. Mineral. Petrol. 171, 1–25. https://doi.org/10.1007/s00410-016-1274-4.

Mavrogenes, J.H., O'Neill, H.St, 1999. The relative effects of pressure, temperature and oxygen fugacity on the solubility of sulfide in mafic magmas. Geochim. Cosmochim. Acta 63 (7/8), 1173–1180, 1999.

Médard, E., McCammon, C.A., Barr, J.A., Grove, T.L., 2008. Oxygen fugacity, temperature reproducibility, and H_2O contents of nominally anhydrous piston-cylinder experiments using graphite capsules. Am. Mineral. 93, 1838–1844. https://doi.org/10.2138/am.2008.2842.

Métrich, N., Schiano, P., Clocchiatti, R., Maury, R.C., 1999a. The transfer of sulfur in subduction settings: an example from the Batan Island (Luzon volcanic arc, Phillipines). Earth Planet, Sci, Lett 167, 1–14.

Moretti, R., Baker, D.R., 2008. Modeling the interplay of fO_2 and fS_2 along the FeS-silicate melt equilibrium. Chem, Geol 25, 286–298. https://doi.org/10.1016/j.chemgeo.2008.06.055.

Moussallam, Y., Georgeais, G., Rose-Koga, E.F., Koga, K.T., Hartley, M.E., Scaillet, B., Oppenheimer, C., Peters, N., 2023. CO_2-undersaturated melt inclusions from the South West indian ridge record surprisingly uniform redox conditions. Geochem. Geophys. Geosystems 24.

Mungall, J.E., 2002. Roasting the mantle: slab melting and the genesis of major Au and Au-rich Cu deposits. Geology 30, 915–918.

Muth, M.J., Wallace, P.J., 2021. Slab-derived sulfate generates oxidized basaltic magmas in the southern Cascade arc (California, USA). Geology 49 (10), 1177–1181.

Muth, M.J., Wallace, P.J., 2022. Sulfur recycling in subduction zones and the oxygen fugacity of mafic arc magmas. Earth Planet, Sci, Lett 599.

Muth, M.J., Cottrell, E., 2023. No detectable redox exchange between sulfur and iron during rapid cooling of basalts. Earth Planet, Sci, Lett 616.

Naldrett, A.J., Duke, J.M., 1980. Platinum metals in magmatic sulfide ores. Sience 208, 1417–1424.

Nash, W.M., Smythe, D.J., Wood, B.J., 2019. Compositional and temperature effects on sulfur speciation and solubility in silicate melts. Earth Planet, Sci, Lett 507, 187–198. https://doi.org/10.1016/j.epsl.2018.12.006.

O'Neill, H.S.C., Berry, A.J., McCammon, C.C., Jayasuriya, K.D., Campbell, S.J., Foran, G., 2006. An experimental determination of the effect of pressure on the $Fe^{3+}/\Sigma Fe$ ratio of an anhydrous silicate melt to 3.0 GPa. Am. Mineral. 91 (2–3), 404–412.

O'Neill, H.S.C., 2021. The thermodynamic controls on sulfide saturation in silicate melts with application to ocean floor basalts. Magma Redox Geochem. 177–213. https://doi.org/10.1002/9781119473206.ch3.

O'Neill, H.S.C., Mavrogenes, J.A., 2022. The sulfate capacities of silicate melts. Geochim Cosmochim Acta 334, 368–382. https://doi.org/10.1016/j.gca.2022.06.020.

Peach, C.L., Mather, T.A., Keays, R.R., 1990. Sulfide melt-silicate distribution coefficients for noble metals and other chalcophile elements as deduced from MORB: implications for partial melting. Geochem. Cosm. Acta 54, 3379–3389.

Raghavan, V., 2004. Fe-Pt-S (Iron-Platinum-Sulfur). J. Ph. Equilibria Diffus. 25, 279–281. https://doi.org/10.1361/15477030419586.

Richards, J.P., 2015. The oxidation state, and sulfur and Cu contents of arc magmas : implications for metallogeny. Lithos 233, 27–45. https://doi.org/10.1016/j.lithos.2014.12.011.

Rezeau, H., Jagoutz, O., 2020. The importance of H_2O in arc magmas for the formation of porphyry Cu deposits. Ore Geol Rev 126.

Rowe, M.C., Kent, A.J.R., Nielsen, R.L., 2009. Subduction influence on oxygen fugacity and trace and volatile elements in basalts across the Cascade volcanic arc. J. Petrol. 50, 61–91.

Saper, L.M., Baker, M.B., Brounce, M., Hughes, E.C., Hofmann, A.E., Stolper, E.M., 2024a. Experimental constraints on iron and sulfur redox equilibria and kinetics in basaltic melt inclusions. Geochim. Cosmochim. Acta 381, 75–96.

Saper, L.M., Brounce, M., Woelki, D., Cao, R., Bromiley, G., 2024b. Variable oxidizing capacity of slab-derived fluids: insights from Fe and S speciation in glasses from the Troodos Ophiolite. Earth Planet, Sci, Lett 627, 118560.

Sorbadere, F., Laurenz, V., Frost, D.J., Wenz, M., Rosenthal, A., McCammon, C., Rivard, C., 2018. The behaviour of ferric iron during partial melting of peridotite. Geochim. Cosmochim. Acta 239, 235–254.

Stolper, E.M., Shorttle, O., Antoshechkina, P.M., Asimow, P.D., 2020. The effects of solid-solid phase equilibria on the oxygen fugacity of the upper mantle. Am. Mineral. 105, 1445–1471.

Till, C.B., 2017. A review and update of mantle thermobarometry for primitive arc magmas. Am. Mineral. 102, 931–947.

Wallace, P.J., Carmichael, I.S.E., 1994. S speciation in submarine basaltic glasses as determined by measurements of S kα X-ray wavelength shifts. Am. Mineral. 79, 161–167.

Walker, D., DeLong, S.E., 1982. Soret separation of mid-ocean ridge basalt magma. Contrib. Mineral. Petrol. 79, 231–240. https://doi.org/10.1007/BF00371514.

Zhang, H.L., Cottrell, E., Solheid, P.A., Kelley, K.A., Hirschmann, M.M., 2018. Determination of $Fe^{3+}/\Sigma Fe$ of XANES basaltic glass standards by Mössbauer spectroscopy and its application to the oxidation state of iron in MORB. Chem. Geol. 479, 166–175.

Zhang, H.L., Hirschmann, M.M., Cottrell, E., Withers, A.C., 2017. Effect of pressure on $Fe^{3+}/\Sigma Fe$ ratio in a mafic magma and consequences for magma ocean redox gradients. Geochim. Cosmochim. Acta 204, 83–103.